Engineered Science
DOI: https://dx.doi.org/10.30919/es952

# Anisotropic Thermal Transport in Chalcogenide Perovskite $CaZrS_3$ from Machine Learning Interatomic Potential

Yinglei Wang,[1, 2] Jialin Tang,[2, 3] Guotai Li,[1, 2] Jiongzhi Zheng,[4] Xiaohan Song,[2] Qi Wang,[2] Zheng Cui,[1, 2] Lin Cheng[2,*] and Ruiqiang Guo[2,*]

## Abstract

Chalcogenide perovskites are being actively considered for photovoltaic, optoelectronic, and thermoelectric applications due to their high carrier mobility, strong light absorption, long-term stability, and environment-friendliness. For all these applications, thermal properties play a key role in determining the performance and lifetime of perovskite systems. In this work, we have developed a machine-learning Gaussian approximation potential to study the structural and thermal transport properties of chalcogenide perovskite $CaZrS_3$. We show that the GAP achieves a DFT-level accuracy in describing both cubic and orthorhombic $CaZrS_3$, with 2-4 orders of magnitude reduced computational cost. Specifically, we applied the GAP to predict the lattice thermal conductivities ($\kappa_L$) and phonon properties of orthorhombic $CaZrS_3$ from 200 to 900 K by considering four-phonon processes. Compared to its counterpart $CaZrSe_3$, the $CaZrS_3$ exhibits comparably low but relatively more anisotropic $\kappa_L$ mainly due to its strong anharmonicity and anisotropic group velocities. Specifically, its thermal conductivities along the *a*- and *c*-axis are close and notably lower than that along the *b*-axis. Optical phonons contribute as high as nearly half of the total thermal conductivity throughout the entire temperature range. Particularly, we observe non-negligible suppression of $\kappa_L$ by four-phonon scattering, which is 10% at 300 K and increases to 23% at 900 K. The four-phonon scattering is dominated by the redistribution process, which has a large phase space comparable to that of three-phonon processes within the most frequency range. These results provide a thorough understanding of the phonon transport in orthorhombic $CaZrS_3$ and will be helpful for tailoring the thermal properties and thus the performance of perovskites for potential applications.

*Keywords:* Anisotropic thermal conductivity; Phonon transport; Machine learning interatomic potential; Four-phonon scattering; Chalcogenide perovskites.
Received: 07 August 2023; Revised: 28 August 2023; Accepted: 30 August 2023.
Article type: Research article.

## 1. Introduction

Chalcogenide perovskites have received growing interest recently due to their high carrier mobility, strong light absorption, long-term stability, and environment-friendliness.[1-3] These extraordinary properties make them particularly attractive for photovoltaic, optoelectronic, and thermoelectric applications.[4-6] For example, $NH_3NH_3ZrS_3$ with a direct band gap of 1.68 eV has been reported to have a high theoretical photoelectric efficiency of about 29%.[7] Promising optoelectronic properties have been found in $BaZrS_3$ nanoparticles with photoluminescence decay times of 4.7 ns.[8] $CaZrSe_3$ as a thermoelectric material has been predicted to possess a high dimensionless figure of merit *ZT* of ~1 at 600 K due to the low thermal conductivity and high Seebeck coefficient.[6,9]

For all these applications, thermal properties play a key role in determining the efficiency, stability, and life of perovskite systems.[10,11] Particularly, solar cells best work between 20 and 35 °C, and overheating will decrease their power generation efficiency and long-term stability.[12] However, perovskites typically have a low thermal conductivity of 1 to 10 $Wm^{-1}K^{-1}$,[13-15] which can prevent heat conduction and bring more risks of overheating. In typical

[1] *Institute of Thermal Science and Technology, Shandong University, Jinan, Shandong 250061, China.*
[2] *Thermal Science Research Center, Shandong Institute of Advanced Technology, Jinan, Shandong 250103, China.*
[3] *Institute of Advanced Technology, Shandong University, Jinan, Shandong 250061, China.*
[4] *Thayer School of Engineering, Dartmouth College, Hanover, New Hampshire 03755, USA.*
**Email:* cheng@sdu.edu.cn (L. Cheng); ruiqiang.guo@iat.cn (R. Guo)

LEDs, 70-85% of the input power is dissipated as waste heat, which can cause temperature rise and thus the reduction of output power, forward voltage, and dominant wavelength.[16,17] For thermoelectric applications, low thermal conductivity is expected for high heat-to-electricity conversion efficiency. One of the most efficient strategies to improve *ZT* is to suppress the phonon contributions ($\kappa_L$) to $\kappa$ while preserving the power factor $S^2\sigma$,[18] which has been demonstrated for PbTe,[19] SnSe,[20] GeTe[21] and $Bi_{0.5}Sb_{1.5}Te_3$,[22] *etc.*

Due to the importance of thermal effects for the aforementioned applications, several works have been done to investigate the thermal properties of chalcogenide perovskites.[6,23-25]. Eric *et al.* predicted a low $\kappa_L$ of 1.16 $Wm^{-1}K^{-1}$ in $BaZrS_3$[23] at 300 K using *first-principles* calculations combined with the Peierls-Boltzmann transport equations (PBTE), which is mainly attributed to its strong anharmonicity. Using the same approach, Hatef et al. obtained isotropic $\kappa_L$ (1.8 $Wm^{-1}K^{-1}$ at 300 K) in distorted $BaHfS_3$ but strongly anisotropic $\kappa_L$ in $SnHfS_3$ (1.7 $Wm^{-1}K^{-1}$ for $\kappa_b$ while 5 $Wm^{-1}K^{-1}$ for $\kappa_a$ at 300 K).[24] Nicholas et al. observed a reduction of $\kappa_L$ from 0.9 to 0.77 $Wm^{-1}K^{-1}$ in $SrHfSe_3$ by substituting 1 mol% Sb for Sr at 700 K using the laser flash method.[25]

Despite the progress, deeper insights into thermal transport in chalcogenide perovskites are highly desired for further manipulating their thermal properties. Understanding thermal transport in solid materials essentially requires a microscopic view of heat carriers, which are often obtained by atomistic simulations.[26-28] Because conventionally used simulations based on density functional theory (DFT) and empirical potentials suffer from high computational costs and low accuracy, respectively, it is challenging to use these approaches to simulate complex materials such as chalcogenide perovskites.[29,30] Recently, machine learning interatomic potentials (MLIPs) are emerging as a powerful tool to bridge the gap between DFT and empirical potentials.[31-34] Several MLIPs have been successfully constructed, such as the Gaussian approximation potential (GAP),[35-40] the spectral neighbor analysis potential (SNAP),[41,42] the neural-network potential (NNP),[43-46] the moment tensor potential (MTP),[47,48] and the deep potential,[49-51] demonstrating that MLIPs can achieve a DFT-level accuracy with orders of magnitude reduced computational cost. Most of these MLIPs have been developed for mono-elemental materials and binary compounds, while those for describing materials with three or more elements have been rarely reported.

In this work, we developed a single GAP that can accurately model phonon transport in both cubic and orthorhombic $CaZrS_3$ with a DFT-level accuracy. Specifically, we applied the GAP combined with the PBTE to predict the $\kappa_L$ and phonon transport properties of the orthorhombic $CaZrS_3$ from 200 to 900 K by considering both three- and four-phonon processes. The orthorhombic $CaZrS_3$ exhibits similarly low but more anisotropic $\kappa_L$ compared to its counterpart $CaZrSe_3$, which is mainly attributed to strong anharmonicity and anisotropic group velocities. The anisotropic and low $\kappa_L$ of $CaZrS_3$ is featured by its short phonon mean free path (MFP), with a value of 4.6, 9.8, and 5.6 nm corresponding to 50% cumulative $\kappa_L$ at 300 K along *a*-, *b*-, and *c*-axis, respectively. Particularly, the contribution of optical phonons to $\kappa_L$ is as high as ~50% throughout the entire temperature range along each direction. Compared with the three-phonon-only calculation, further considering the four-phonon scattering process decreases the $\kappa_L$ of $CaZrS_3$ by 10% at 300 K and up to 23% at 900 K, indicating the non-negligible influence of the four-phonon scattering. The redistribution process dominates the four-phonon scattering because of its large phase space which is close to that of three-phonon processes within most frequency range. Our work demonstrates the ability of GAP to predict the thermal transport properties of ternary compounds with a DFT-level accuracy and 2-4 orders of magnitude reduced computational cost. The insights gained into phonon transport of orthorhombic $CaZrS_3$ will be helpful for tailoring the thermal properties and thus the performance of perovskites used for photovoltaics, optoelectronics, thermoelectrics, etc.

## 2. Methods

### 2.1 GAP calculation

Gaussian approximation potentials are constructed by fitting the Born-Oppenheimer potential energy surface (PES) based on Gaussian process regression.[35,52-54] The total energy of a system for the present GAP consists of two-body (2*B*), three-body (3*B*), and many-body (M*B*) interactions.[53,54]:

$$E = \delta^{2B}\sum_{ij}\epsilon^{2B}\left(\mathbf{q}_{ij}^{2B}\right) + \delta^{3B}\sum_{ijk}\epsilon^{3B}\left(\mathbf{q}_{ijk}^{3B}\right) + \delta^{MB}\sum_{i}\epsilon^{MB}\left(\mathbf{q}_{i}^{MB}\right), \quad (1)$$

where *i*, *j* and *k* represent the atomic indices in the system, $\delta$ represents the weighting factor, $\mathbf{q}$ is an atomic environment descriptor. The local atomic energy contribution $\epsilon^d(\mathbf{q}_i^d)$ is a linear combination of each kernel functions $K^d$ for the descriptor *d*:

$$\epsilon^d\left(\mathrm{q}_i^d\right) = \sum_{t=1}^{N_t^d}\alpha_t^d\, K^d\left(\mathrm{q}_i^d, \mathrm{q}_t^d\right), \quad (2)$$

where $N_t$ is the number of basis functions, $\alpha_t$ is a weight coefficient obtained during the fitting process, and $K^d$ is the kernel function measuring the similarity between pre-observed atomic environment $\mathbf{q}_t^d$ and the to-be-predicted atomic environment $\mathbf{q}_i^d$. The 2*B* descriptor is simply the interatomic distances:

$$q_{ij}^{2B} = \left|\mathbf{r}_j - \mathbf{r}_i\right| \equiv r_{ij}, \quad (3)$$

where $\mathbf{r}_i$ is the position of atom *i*. The 3*B* descriptor which has a symmetrized transformation of the Cartesian coordinates is:

$$\mathbf{q}_{ijk}^{3B} = \begin{pmatrix} r_{ij} + r_{ik} \\ \left(r_{ij} - r_{ik}\right)^2 \\ r_{jk} \end{pmatrix}. \quad (4)$$

In this work, we use the smooth overlap of atomic positions (SOAP)[55,56] to describe many-body interactions, in which the atomic environment of the *i*th-atom is represented by the local atomic neighbor density $\rho_i(\mathbf{r})$:

$$\rho_i(\mathbf{r}) = \sum_j f_{\text{cut}}(r_{ij}) \exp\left[-\frac{(\mathbf{r}_i - \mathbf{r}_{ij})^2}{2\sigma_{\text{at}}^2}\right], \quad (5)$$

where $j$ is the neighbor atom within a given cutoff radius ($r_{\text{cut}}$), $\sigma_{\text{at}}$ represents the width of the Gaussian function, and $f_{\text{cut}}$ is a function that goes smoothly to 0 at the cutoff distance. The local atomic neighbor density can be expanded in a basis set of the radial function $g_n(r)$ and spherical harmonic function $Y_{lm}(\mathbf{r})$ multiplied by the expansion coefficients $c_{nlm}^{(i)}$:

$$\rho_i(\mathbf{r}) = \sum_{nlm} c_{nlm}^{(i)} g_n(r) Y_{lm}(\mathbf{r}). \quad (6)$$

### 2.2 GAP databases

The training and testing databases consist of DFT energies, atomic forces, and virial stresses of both orthorhombic and cubic $CaZrS_3$ configurations. To generate the training database, we first performed *ab-initio* molecular dynamics (AIMD) simulations for the cubic $CaZrS_3$ using a 3 × 3 × 3 supercell (135 atoms) and a 2 × 2 × 2 k-point grid, as implemented in Vienna Ab initio Simulation Package (VASP).[57] The Perdew-Burke-Ernzerhof (PBE) form of generalized gradient approximation (GGA)[58-60] was used for exchange-correlation functional. The AIMD simulation was run for 2.5 ps with a time step of 0.5 fs under the periodic boundary conditions in the canonical ensemble (*NVT*: constant number of particles *N*, constant volume *V*, and constant temperature *T*) at 300 K. Then, 45 (60) configurations of cubic $CaZrS_3$ were extracted for training (testing) by sampling one snapshot every 50 timesteps.

For the orthorhombic configurations, directly running AIMD simulations using a supercell with a similar size to the cubic case is too expensive because the primitive cell of the orthorhombic structure (20 atoms) contains more atoms than the cubic one (5 atoms). Therefore, we choose to develop an initial GAP of low accuracy and use it to generate configurations of orthorhombic $CaZrS_3$. To train an initial GAP, we used orthorhombic $CaZrS_3$ configurations of a 2 × 2 × 2 supercell to perform an AIMD simulation only at the gamma point in the *NVT* ensemble at 300K. The simulation length was 5 ps with a time step of 0.5 fs. We extracted 100 orthorhombic $CaZrS_3$ configurations by sampling one snapshot every 50 timesteps and trained the initial GAP with a cutoff radius of 5.0 Å. In a similar way, we used this initial GAP to perform a MD simulation with a 3 × 3 × 2 supercell in the *NVT* ensemble at 300 K for 5 ps with a timestep of 0.5 fs via LAMMPS,[61] which has been widely used for various systems.[62-65] We extracted 35 (57) orthorhombic configurations from the MD simulation to construct the training (testing) dataset.

After obtaining all the orthorhombic and cubic configurations, self-consistent field (SCF) calculations were performed to obtain energies, atomic forces, and virial stresses using VASP. The energy convergence for both AIMD and SCF calculations was set to $10^{-8}$ eV/atom. Finally, we trained the GAP using the 80 configurations (45 cubic and 35 orthorhombic) with a cutoff of 7.0 Å for the 2*B*, 3*B*, and SOAP descriptors.

### 2.3 Thermal conductivity calculation

Within the framework of the Peierls-Boltzmann transport equation (PBTE), the lattice thermal conductivity can be written as

$$\kappa_L^{\alpha\beta} = \frac{1}{k_B T^2 \Omega N} \sum_\lambda n_\lambda^0 (n_\lambda^0 + 1)(\hbar\omega_\lambda)^2 v_\lambda^\alpha F_\lambda^\beta, \quad (7)$$

where $k_B$ is the Boltzmann constant, $T$ is the temperature, $\Omega$ is the volume of the unit cell, $N$ represents the total number of sampled phonon wave vectors in the first Brillouin zone, $n_\lambda^0$ is the equilibrium phonon Bose-Einstein distribution, and $\hbar$ is the reduced Planck constant. $\omega_\lambda$ and $\mathbf{v}_\lambda$ are the frequency and group velocity of each phonon mode $\lambda$, respectively. $\mathbf{F}$ is the linear phonon perturbation vector, and can be calculated by iteratively solving the PBTE. $\mathbf{F}_\lambda = \tau_\lambda^0(\mathbf{v}_\lambda + \Delta_\lambda)$, where $\tau_\lambda^0$ is the relaxation time and the $\Delta_\lambda$ term takes into account coupling of nonequilibrium $\lambda$ phonon modes to other phonon modes based on energy and momentum conservation. According to the Matthiessen's rule, the phonon relaxation time of mode $\lambda$ within single-mode relaxation time approximation (SMRTA) $\tau_\lambda^0$ can be expressed as

$$\frac{1}{\tau_\lambda^0} = \frac{1}{N}\left[\sum_{\lambda'\lambda''}^{(+)} \Gamma_{\lambda\lambda'\lambda''}^{(+)} + \sum_{\lambda'\lambda''}^{(-)} \frac{1}{2}\Gamma_{\lambda\lambda'\lambda''}^{(-)}\right] + \frac{1}{N}\sum_{\lambda'}^{(iso)} \Gamma_{\lambda\lambda'}^{(iso)} + \frac{1}{N}\left[\sum_{\lambda'\lambda''\lambda'''}^{(++)} \frac{1}{2}\Gamma_{\lambda\lambda'\lambda''\lambda'''}^{(++)} + \sum_{\lambda'\lambda''\lambda'''}^{(+-)} \frac{1}{2}\Gamma_{\lambda\lambda'\lambda''\lambda'''}^{(+-)} + \sum_{\lambda'\lambda''\lambda'''}^{(--)} \frac{1}{6}\Gamma_{\lambda\lambda'\lambda''\lambda'''}^{(--)}\right], \quad (8)$$

The superscripts $(+,-)$ or $(++,+-,--)$ denote the three-phonon and four-phonon scattering processes, i.e., $\mathrm{q}'' = \mathrm{q} \pm \mathrm{q}' + \mathrm{Q}$ and $\mathrm{q}''' = \mathrm{q} \pm \mathrm{q}' \pm \mathrm{q}'' + \mathrm{Q}$, respectively, where q is the phonon wave vector and Q is a reciprocal lattice vector. The three-phonon and four-phonon scattering rates $\Gamma$ in Eq. (8) take the form of

$$\Gamma_{\lambda\lambda'\lambda''}^{(+)} = \frac{\hbar\pi}{4}\frac{n_{\lambda'}^0 - n_{\lambda''}^0}{\omega_\lambda \omega_{\lambda'} \omega_{\lambda''}} \left|V_{\lambda\lambda'\lambda''}^{(+)}\right|^2 \delta(\omega_\lambda + \omega_{\lambda'} - \omega_{\lambda''})$$

$$\Gamma_{\lambda\lambda'\lambda''}^{(-)} = \frac{\hbar\pi}{4}\frac{n_{\lambda'}^0 + n_{\lambda''}^0 + 1}{\omega_\lambda \omega_{\lambda'} \omega_{\lambda''}} \left|V_{\lambda\lambda'\lambda''}^{(-)}\right|^2 \delta(\omega_\lambda - \omega_{\lambda'} - \omega_{\lambda''}), \quad (9)$$

$$\Gamma_{\lambda\lambda'\lambda''\lambda'''}^{(++)} = \frac{\hbar^2\pi}{8N_0} \times \frac{(1 + n_{\lambda''}^0)(1 + n_{\lambda'''}^0) n_{\lambda'''}^0}{n_\lambda^0} \times \left|V_{\lambda\lambda'\lambda''\lambda'''}^{(++)}\right|^2 \times \frac{\delta(\omega_\lambda + \omega_{\lambda'} + \omega_{\lambda''} - \omega_{\lambda'''})}{\omega_\lambda \omega_{\lambda'} \omega_{\lambda''} \omega_{\lambda'''}}$$

$$\Gamma_{\lambda\lambda'\lambda''\lambda'''}^{(+-)} = \frac{\hbar^2\pi}{8N_0} \times \frac{(1 + n_{\lambda'}^0) n_{\lambda''}^0 n_{\lambda'''}^0}{n_\lambda^0} \times \left|V_{\lambda\lambda'\lambda''\lambda'''}^{(+-)}\right|^2 \times \frac{\delta(\omega_\lambda + \omega_{\lambda'} - \omega_{\lambda''} - \omega_{\lambda'''})}{\omega_\lambda \omega_{\lambda'} \omega_{\lambda''} \omega_{\lambda'''}}$$

$$\Gamma_{\lambda\lambda'\lambda''\lambda'''}^{(--)} = \frac{\hbar^2\pi}{8N_0} \times \frac{n_{\lambda'}^0 n_{\lambda''}^0 n_{\lambda'''}^0}{n_\lambda^0} \times \left|V_{\lambda\lambda'\lambda''\lambda'''}^{(--)}\right|^2 \times \frac{\delta(\omega_\lambda - \omega_{\lambda'} - \omega_{\lambda''} - \omega_{\lambda'''})}{\omega_\lambda \omega_{\lambda'} \omega_{\lambda''} \omega_{\lambda'''}}, \quad (10)$$

where $V_{\lambda\lambda'\lambda''}$ and $V_{\lambda\lambda'\lambda''\lambda'''}$ denote the three-phonon and four-phonon scattering matrix elements, which are expressed as

$$V_{\lambda\lambda'\lambda''}^{(\pm)} = \sum_{ijk}\sum_{\alpha\beta\gamma} \Phi_{ijk}^{\alpha\beta\gamma} \frac{e_\alpha^\lambda(i) e_\beta^{\pm\lambda'}(j) e_\gamma^{-\lambda''}(k)}{\sqrt{\bar{M}_i \bar{M}_j \bar{M}_k}} e^{\pm i\mathbf{q}'\cdot\mathbf{r}_j} e^{-i\mathbf{q}''\cdot\mathbf{r}_k}, \quad (11)$$

$$V^{(\pm\pm)}_{\lambda\lambda'\lambda''\lambda'''} = \sum_{ijkl}\sum_{\alpha\beta\gamma\theta}\Phi^{\alpha\beta\gamma\theta}_{ijkl}\frac{e^{\lambda}_{\alpha}(i)e^{\pm\lambda'}_{\beta}(j)e^{\pm\lambda''}_{\gamma}(k)e^{-\lambda'''}_{\gamma}(l)}{\sqrt{\bar{M}_i\bar{M}_j\bar{M}_k\bar{M}_l}}e^{\pm i\mathbf{q}'\cdot\mathbf{r}_j}e^{\pm i\mathbf{q}''\cdot\mathbf{r}_k}e^{-i\mathbf{q}'''\cdot\mathbf{r}_l}, \quad (12)$$

where $i$, $j$, $k$, $l$ denote the atomic indices and $\alpha$, $\beta$, $\gamma$, $\theta$ denote the Cartesian directions $x$, $y$, $z$. $\Phi^{\alpha\beta\gamma}_{ijk}$ and $\Phi^{\alpha\beta\gamma\theta}_{ijkl}$ are the third-order and fourth-order interatomic force constants (IFCs), respectively. $e^{q}_{\alpha}(i)$ is the eigenvector component. $\mathbf{r}_j$ is the position vector of the unit cell where $j$-th atom lies, and $M_j$ is its mass. The isotopic scattering rate is given by

$$\Gamma^{(iso)}_{\lambda\lambda'} = \frac{\pi\omega^2}{2}\sum_{i\in u.c.} g(i)|\mathbf{e}^{*}_{\lambda}(i)\cdot\mathbf{e}_{\lambda'}(i)|^2\delta(\omega_{\lambda}-\omega_{\lambda'}), \quad (13)$$

where the mass variance is defined as $g(i)=\sum_s f_s(i)[1-M_s(i)/\bar{M}(i)]^2$. The $f_s(i)$ and $M_s(i)$ are the concentration and mass of the $s$th isotope of atom $i$, respectively. $\bar{M}(i)$ is the average mass of the $i$th atom in the unit cell.

The $\kappa_L$ of orthorhombic $CaZrS_3$ considering only three-phonon scattering is calculated by iteratively solving the linearized PBTE with a 7 × 7 × 7 **q**-mesh, as implemented in ShengBTE.[66] As shown in Fig. S2, a **q**-mesh of 7 × 7 × 7 is large enough to achieve converged value of thermal conductivity. Using the same **q**-mesh, the $\kappa_L$ considering both three- and four-phonon scattering is calculated by iteratively solving the PBTE for three-phonon scattering, with four-phonon scattering treated at the RTA level via the FourPhonon package.[67]

### 2.4 IFC calculations

To obtain the phonon-phonon scattering rates, we use both DFT and GAP to calculate IFCs based on the finite displacement method. The second-order and third-order IFCs were calculated with a 2 × 2 × 2 and a 2 × 2 × 1 supercell, respectively. Considering the high computational cost, the fourth-order IFCs were calculated using only GAP with a 2 × 2 × 1 supercell. The PHONOPY[68] code, thirdorder.py,[66] and fourthorder.py[67] were utilized to construct the displaced configurations for calculating second-order, third-order, and fourth-order IFCs, respectively. The third-order IFCs were calculated up to the fourth nearest neighbor while the fourth-order IFCs were calculated up to the second nearest neighbor. For DFT calculations of cubic and orthorhombic $CaZrS_3$, the VASP code was applied with the PBE form of GGA for the exchange-correlation potential. First, the primitive cells of cubic and orthorhombic $CaZrS_3$ were optimized using a cutoff energy of 560 eV, with the convergence criteria of $10^{-8}$ eV/atom and $10^{-6}$ eV/Å for total energy and atomic forces, respectively. The $k$-points were set to 5 × 5 × 5 for cubic $CaZrS_3$ and 2 × 2 × 2 for orthorhombic $CaZrS_3$, respectively. Then, SCF calculations at the gamma point were performed for calculating atomic forces for each displaced configuration. For GAP calculations, the atomic forces of each configuration were calculated using LAMMPS. For the calculation of phonon dispersion of orthorhombic $CaZrS_3$, the longitudinal optical-transverse optical (LO-TO) splitting was predicted by incorporating the effects of long-range Coulomb interactions based on the Born effective charges (Table SI in Supporting Information) and dielectric constants (Table SII) calculated by Density Functional Perturbation Theory (DFPT).[69]

## 3. Results and discussion

### 3.1 Training the GAP for cubic and orthorhombic $CaZrS_3$

We trained the GAP that can describe both cubic and orthorhombic $CaZrS_3$ using the hyperparameters in Table 1. Most values of the hyperparameters are close to those reported in previous works, except that the $r_{\text{cut}}$ (7.0 Å) is much longer than the commonly used values (typically less than 6 Å).[70,71] This is because the interatomic interaction in $CaZrS_3$ is very long-ranged, as will be shown in Fig. 4. In order to determine the appropriate $r_{\text{cut}}$ for GAP training, we test the convergence of the GAP model with respect to the cutoff radius. Here, we evaluate the accuracy of the GAP model using the root-mean-squared errors (RMSEs) of energies and atomic forces between the GAP and DFT predictions. As shown in Fig. 1, the energies and atomic forces in orthorhombic and cubic $CaZrS_3$ reach converged values at ~6.5 Å and ~7.0 Å, respectively. As a comparison, the cutoff radius is only 3.7 Å for diamond[70] and 4.8 Å for silicon.[70] We also test the accuracy of the GAP model with respect to $n_{max}$ and $l_{max}$, as shown in Fig. S1 (see Supporting Information), showing that the RMSE of atomic forces reaches converged values at $n_{max}/l_{max}=8$.

**Table 1.** Hyperparameter settings for training GAP.

| Hyperparameters | 2*B* | 3*B* | SOAP |
|---|---|---|---|
| $\boldsymbol{\delta}$ (eV) | 10.0 | 3.7 | 0.07 |
| Sparse method | Uniform | Uniform | CUR |
| Sparse points | 50 | 200 | 650 |
| $\boldsymbol{r_{cut}}$ (Å) | 7.0 | 7.0 | 7.0 |
| $\Delta\boldsymbol{r}$ (Å) | - | - | 1 |
| $\boldsymbol{n_{max}}$ | - | - | 8 |
| $\boldsymbol{l_{max}}$ | - | - | 8 |
| $\boldsymbol{\sigma_v^{energy}}$ (eV/atom) | | 0.001 | |
| $\boldsymbol{\sigma_v^{force}}$ (eV/Å) | | 0.0005 | |
| $\boldsymbol{\sigma_v^{virial}}$ (eV/atom) | | 0.001 | |

Figures 2 and 3 further compare the energies and atomic forces of the orthorhombic and cubic $CaZrS_3$ calculated by the GAP and DFT for both the training and testing databases. Our calculations show that the energies and atomic forces predicted by the GAP and DFT are all in good agreement for both orthorhombic and cubic $CaZrS_3$. For orthorhombic $CaZrS_3$, the RMSEs of energy and atomic force on Ca, Zr, and S atoms are 0.73 meV/atom, 0.023, 0.045, and 0.03 eV/Å for the training set, respectively (Fig. 2(a)). The RMSEs of energy (0.79 meV/atom) and atomic force (0.03, 0.052, and 0.031 eV/Å on Ca, Zr, and S atoms, respectively) for the testing set are comparable to those for the training set, suggesting the high accuracy of our GAP in predicting the unlearned configurations of orthorhombic $CaZrS_3$. Compared to the

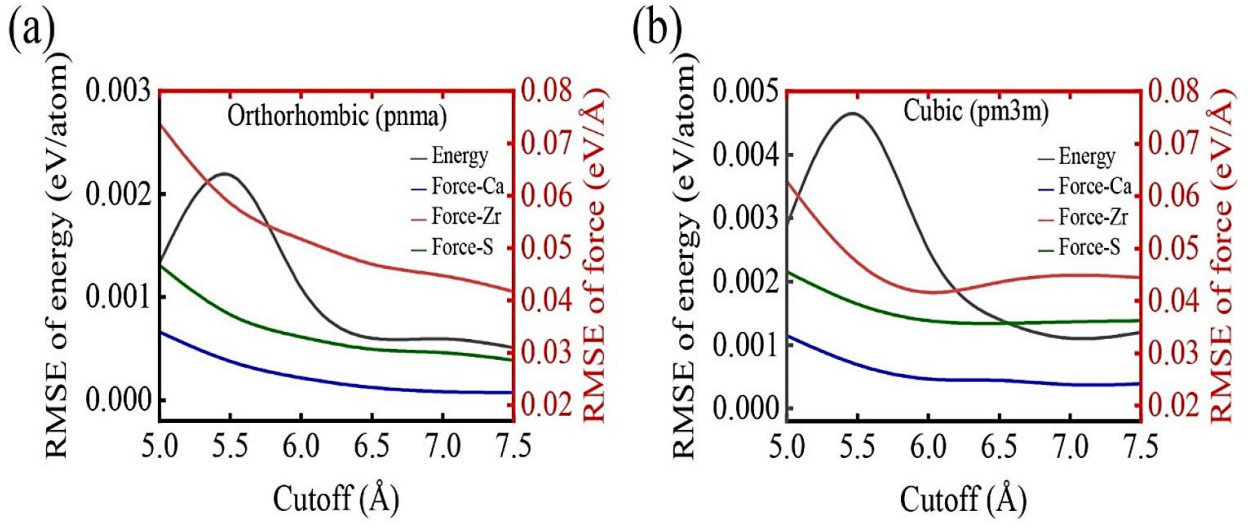


**Fig. 1** Convergence tests of the GAP model with respect to cutoff radius.

orthorhombic $CaZrS_3$, the cubic $CaZrS_3$ exhibits relatively larger RMSEs for both training and testing sets. As shown in Fig. 3, the RMSEs of energy are 2.02 meV/atom for the training set and 1.85 meV/atom for the testing set. In contrast to the orthorhombic $CaZrS_3$, the cubic $CaZrS_3$ exhibits notably larger RMSEs of atomic forces for the testing set (0.040, 0.068, and 0.046 eV/Å for Ca, Zr, and S atoms, respectively) than those for the training set (0.024, 0.045 and 0.036 eV/Å for Ca, Zr and S atoms, respectively). The relatively larger RMSEs for cubic $CaZrS_3$ can be attributed to its weaker interatomic interactions as compared to the orthorhombic one, making it more difficult for the GAP to precisely predict the atomic forces. As later will be shown in Fig. 4, the second-order IFCs of orthorhombic $CaZrS_3$ are generally much larger than those of the cubic one. For example, the self-interaction IFC of the Ca atom for orthorhombic $CaZrS_3$ (6.6 eV/Å$^2$) is four times larger than that for cubic $CaZrS_3$ (1.6 eV/Å$^2$) based on DFT calculations. Overall, the RMSEs of atomic force in orthorhombic and cubic $CaZrS_3$ are comparable to previously reported results for many other materials, e.g., the RMSEs of atomic force is 0.1 eV/Å for a GAP model of diamond,[70] 0.01 eV/Å for a neural network potential of Si,[72] and 0.0197 eV/Å for a moment tensor potential of BAs.[73]

After preliminary evaluating the accuracy of GAP using RMSEs, we calculated the lattice parameters of cubic and orthorhombic $CaZrS_3$ using this GAP. As shown in Table 2, the lattice constants of both the orthorhombic and cubic $CaZrS_3$ predicted by GAP show good agreement with the DFT

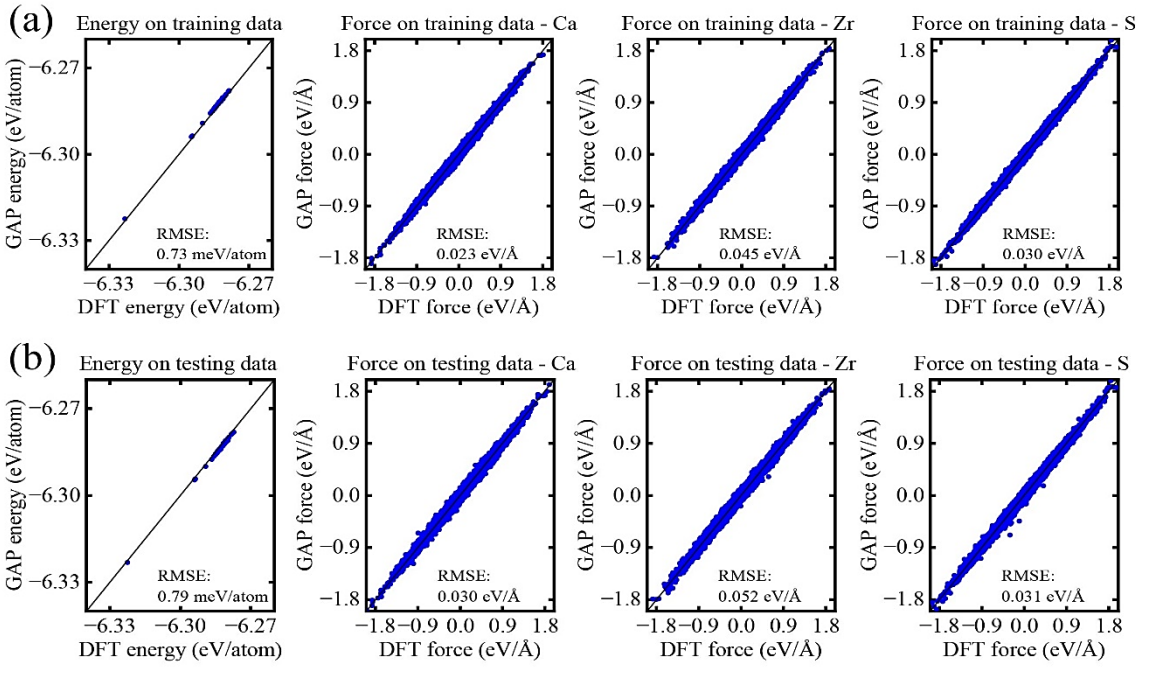


**Fig. 2** Prediction accuracy of the GAP for energies and atomic forces on Ca, Zr, and S atoms of orthorhombic $CaZrS_3$. GAP versus DFT predictions for the (a) training and (b) testing databases.

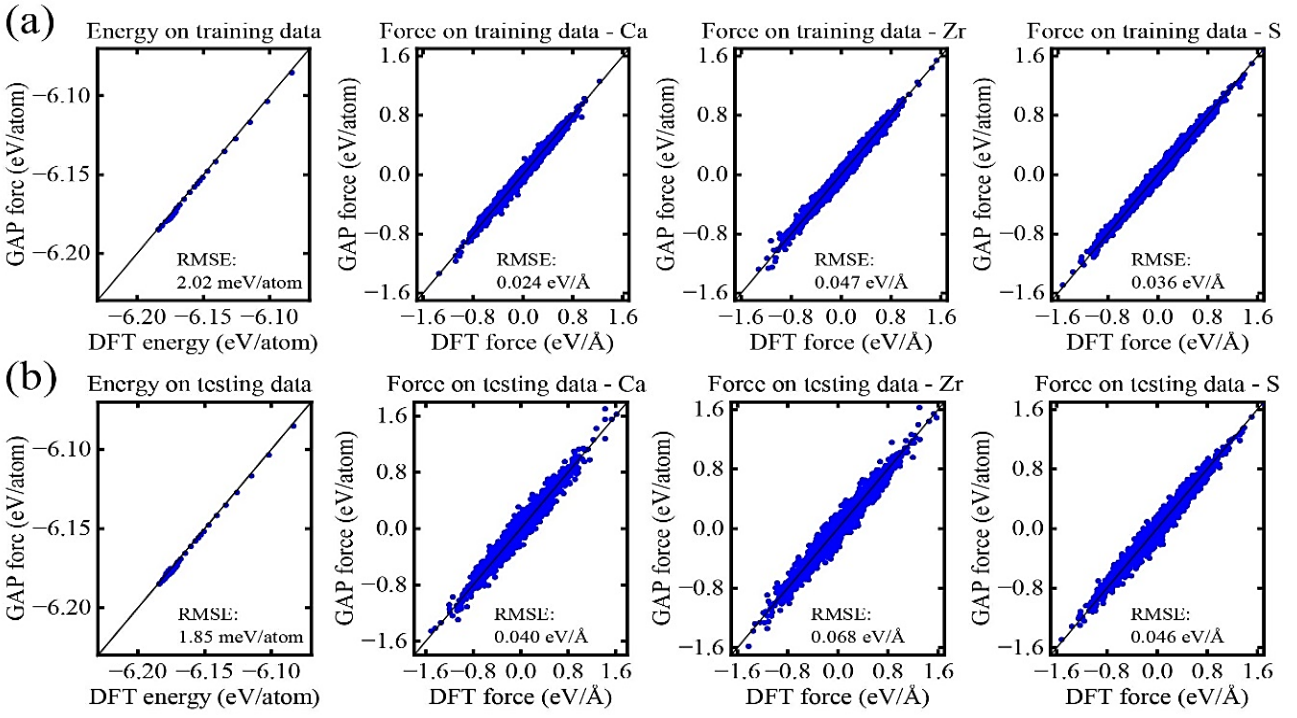


**Fig. 3** Prediction accuracy of the GAP for energies and atomic forces on Ca, Zr, and S atoms of cubic $CaZrS_3$. GAP versus DFT predictions for the (a) training and (b) testing databases.

**Table 2.** The lattice parameters of orthorhombic (pnma) and cubic (pm3m) $CaZrS_3$ predicted by using GAP, in comparison with DFT and experimental results.

| Phase | Method | *a* (Å) | *b* (Å) | *c* (Å) | Volume (Å$^3$) |
|---|---|---|---|---|---|
| Pnma | GAP | 7.072 | 9.649 | 6.573 | 448.57 |
| | DFT (PBE, this work) | 7.070 | 9.645 | 6.578 | 448.60 |
| | DFT (PBE)[83] | 7.072 | 9.661 | 6.582 | 449.68 |
| | Experiment[84] | 7.030 | 9.589 | 6.573 | 440.66 |
| Pm3m | GAP | 4.984 | | | 123.82 |
| | DFT (PBE, this work) | 4.979 | | | 123.44 |
| | DFT (PBE)[83] | 4.980 | | | 123.51 |

results. Specifically, the lattice constants of orthorhombic $CaZrS_3$ calculated by the GAP and DFT differ by ~0.04%, and the volumes differ by ~0.006%. Meanwhile, both the GAP and DFT results agree well with the experimental values for orthorhombic $CaZrS_3$. For cubic $CaZrS_3$, the GAP and DFT results differ by ~0.1% for the lattice constants and ~0.3% for the volume, which are relatively larger compared to the orthorhombic case.

We continue to evaluate the accuracy of the GAP in predicting IFCs of both orthorhombic and cubic $CaZrS_3$, which essentially determine their phonon properties and lattice thermal conductivity. Fig. 4 compares the second-order IFCs calculated by the GAP and DFT as a function of interatomic distance. The IFCs predicted by GAP are generally consistent

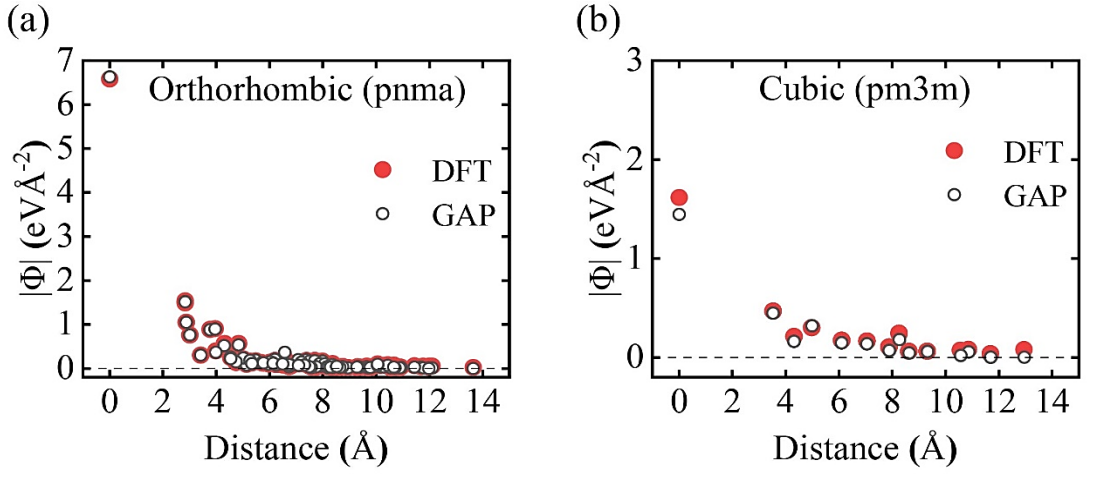


**Fig. 4** Prediction accuracy of the GAP for second-order IFCs. The second-order IFCs calculated by DFT and GAP as a function of the interatomic distance from a central Ca atom for (a) orthorhombic and (b) cubic $CaZrS_3$.

with the DFT results. Specifically, the maximum deviation of second-order IFCs is 0.053 eV/Å$^2$ for orthorhombic $CaZrS_3$ and 0.093 eV/Å$^2$ for cubic $CaZrS_3$. The RMSE of second-order IFCs is 0.021 eV/Å$^2$ for orthorhombic $CaZrS_3$ and 0.036 eV/Å$^2$ for cubic $CaZrS_3$. As expected, the RMSE of second-order IFCs for cubic $CaZrS_3$ is relatively larger than that of the orthorhombic one considering the relatively larger RMSEs of atomic forces in the former.

Figure 5 further shows the anharmonic IFCs calculated by the GAP and DFT. In this work, we select several representative third-order IFCs to test the accuracy of third-order IFCs calculated by GAP. The IFCs are calculated by fixing two atoms (the 1st atom and its nearest atom) in the triplets and displacing the third atom at a varying distance. Specifically, we calculate $\Phi^{\alpha,x,x}_{Ca,S,k}$ and $\Phi^{\alpha,x,x}_{S,Zr,k}$ (The subscript $k$ represents the atom index in primitive cell and the superscripts represent the Cartesian axis.) for both orthorhombic and cubic $CaZrS_3$. For the orthorhombic (cubic) phase, the distance between the Ca and S atoms in $\Phi^{\alpha,x,x}_{Ca,S,k}$ is 2.83 Å (3.52 Å) and that between the S and Zr atoms in $\Phi^{\alpha,x,x}_{S,Zr,k}$ is 2.56 Å (2.49 Å). As shown in Fig. 5, the third-order IFCs calculated by GAP agree well with the DFT results for both orthorhombic and cubic $CaZrS_3$. The RMSEs of the third-order IFCs for orthorhombic $CaZrS_3$ are 0.1 eV/Å$^3$ for $\Phi^{\alpha,x,x}_{Ca,S,k}$ (Fig. 5(a)) and 0.07 eV/Å$^3$ for $\Phi^{\alpha,x,x}_{S,Zr,k}$ (Fig. 5(b)), which are comparable to that for the cubic $CaZrS_3$ (0.1 eV/Å$^3$ for $\Phi^{\alpha,x,x}_{Ca,S,k}$ in Fig. 5(c) and 0.09 eV/Å$^3$ for $\Phi^{\alpha,x,x}_{S,Zr,k}$ in Fig. 5(d)). As a comparison, we also show the third-order IFCs calculated by a less accurate GAP named GAP$^0$, which underpredicts the $\kappa_L$ of orthorhombic $CaZrS_3$ by 30% at 300 K. As expected, the GAP$^0$ exhibits substantially larger prediction errors, with a RMSE of 0.63 (0.25) eV/Å$^3$ for $\Phi^{\alpha,x,x}_{Ca,S,k}$ and 0.78 (0.72) eV/Å$^3$ for $\Phi^{\alpha,x,x}_{S,Zr,k}$ of orthorhombic (cubic) $CaZrS_3$. Specifically, our GAP and the GAP$^0$ predict largely different values for the first two values in each IFC. For orthorhombic $CaZrS_3$, the $\Phi^{\alpha,x,x}_{Ca,S,k}$ calculated by the GAP and DFT differ by 0.3% and 1.8% for the first and second values, respectively. Similarly, the predictions by the GAP and DFT differ by 1.9% and 0.7% for the first and second $\Phi^{\alpha,x,x}_{S,Zr,k}$ in the orthorhombic structure, respectively. In contrast, largely different values are observed between the GAP$^0$ and DFT predictions, which differ by 40% (30%) and 41% (23%) for the first and second values of $\Phi^{\alpha,x,x}_{Ca,S,k}$ ($\Phi^{\alpha,x,x}_{S,Zr,k}$), respectively. Similarly, the GAP$^0$ shows notably larger errors in predicting the third-order IFCs of the cubic phase.

After validating the accuracy of GAP, we next evaluate its computational efficiency for MD simulations. We compared AIMD and GAP-based MD simulations for a 2 × 2 × 2 supercell of orthorhombic $CaZrS_3$ containing 160 atoms, which were performed in the *NVT* ensemble at 300 K with a timestep of 0.1 fs using the Intel Xeon Gold 6254 CPU (16 cores). The computational cost per time step is 179.4 and 1996.9 s for AIMD simulations based on a 1 × 1 × 1 and 2 × 2 × 2 *k*-mesh, respectively. In contrast, MD simulations based on the GAP costs only 0.5 s for each time step, which is 2-4 orders of magnitude faster than the AIMD simulations.

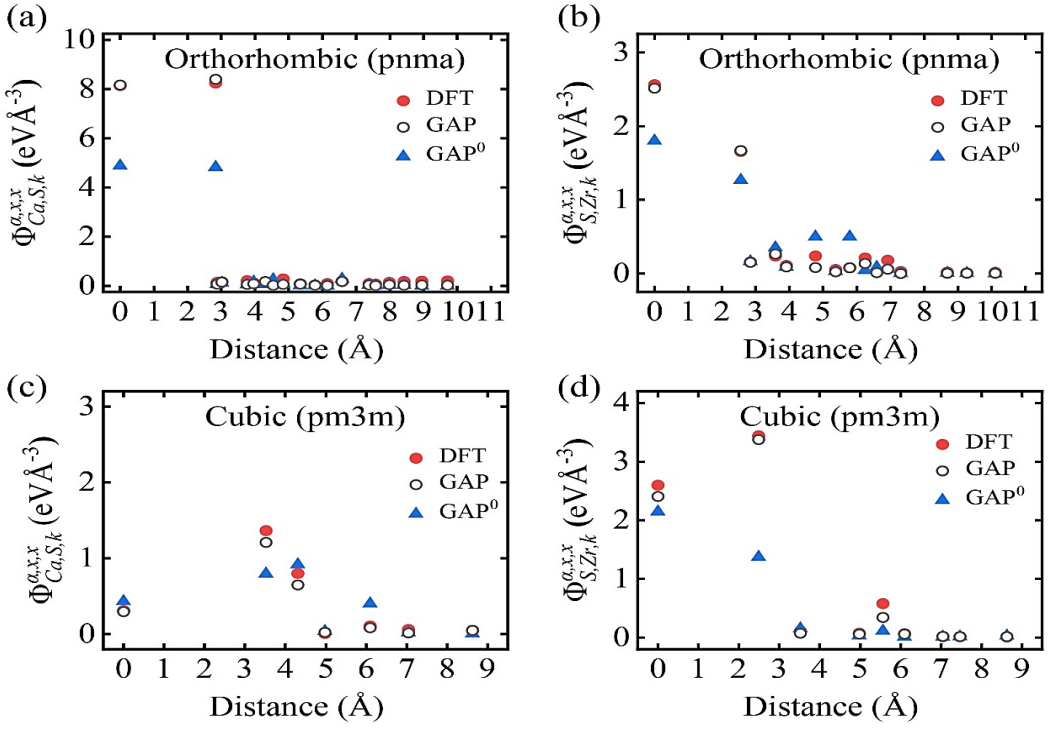


**Fig. 5** Prediction accuracy of the GAP for third-order IFCs of orthorhombic and cubic $CaZrS_3$. The third-order IFCs as a function of interatomic distance for (a) $\Phi^{\alpha,x,x}_{Ca,S,k}$ and (b) $\Phi^{\alpha,x,x}_{S,Zr,k}$ in orthorhombic $CaZrS_3$, as well as (c) $\Phi^{\alpha,x,x}_{Ca,S,k}$ and (d) $\Phi^{\alpha,x,x}_{S,Zr,k}$ in cubic $CaZrS_3$, which are calculated by fixing the first two atoms while displacing the third atom in a triplet. The interatomic distance is the distance between the first and the third atoms.

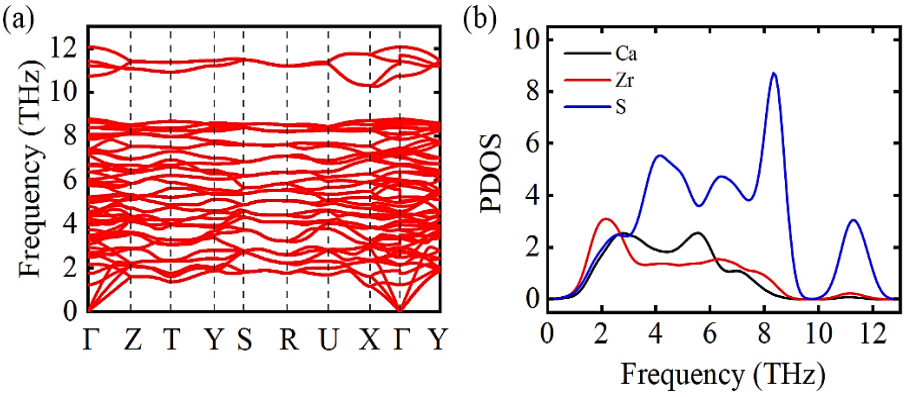


**Fig. 6** Harmonic phonon properties of orthorhombic $CaZrS_3$ calculated by GAP. (a) The phonon dispersion and (b) the partial density of states.

### 3.2 Phonon transport in orthorhombic $CaZrS_3$

The high accuracy of GAP indicates it can achieve a DFT-level accuracy in predicting the phonon transport properties of $CaZrS_3$. In Figs. S3 and S4, we compare the phonon dispersion, phonon partial density of states (PDOS) and thermal conductivity within the three-phonon framework calculated by GAP and DFT, which as expected agree well with each other. After validating the accuracy of GAP, we now use it to study phonon transport properties in $CaZrS_3$. Within the framework of harmonic approximation, negative frequencies are observed in the phonon dispersion of cubic $CaZrS_3$ (Fig. S5), which is expected considering it is a high-temperature phase. Accurately predicting its phonon dispersion and thermal conductivity requires considering anharmonic phonon renormalization, which is much more computationally expensive.[74,75] In this work, we only focus on the phonon properties of orthorhombic $CaZrS_3$ and all these results are calculated using GAP in the subsequent discussion. Fig. 6 shows that its phonon dispersion has no negative frequency, indicating the dynamical stability of orthorhombic $CaZrS_3$. The acoustic phonon branches near the Γ point are much more dispersive than most optical branches, indicating significantly higher group velocities of the acoustic modes. The PDOS in Fig. 6(b) shows that the high-frequency vibrations are mainly contributed by the relatively light S atoms while the heavy Zr atoms contribute most of the low-frequency phonon modes below ~2.6 THz.

Figure 7 shows the temperature-dependent $\kappa_L$ of orthorhombic $CaZrS_3$ from 200 to 900 K, in comparison with its counterpart $CaZrSe_3$. The lattice thermal conductivity considering only three-phonon scattering is denoted by $\kappa_L^{3ph}$ and that considering up to four-phonon scattering is denoted by $\kappa_L^{3ph+4ph}$. As shown in Fig. 7(a), the lattice thermal conductivity of orthorhombic $CaZrS_3$ is very low and slightly anisotropic. Specifically, the $\kappa_a^{3ph+4ph}$ (the subscript represents the lattice direction) and $\kappa_c^{3ph+4ph}$ are close to each other while $\kappa_b^{3ph+4ph}$ is relatively higher. For example, at 300K, its $\kappa_b^{3ph+4ph}$ is 1.68 $Wm^{-1}K^{-1}$ while $\kappa_a^{3ph+4ph}$ is 1.25 $Wm^{-1}K^{-1}$ and $\kappa_c^{3ph+4ph}$ is 1.17 $Wm^{-1}K^{-1}$. In comparison, the $\kappa_L$ of its counterpart $CaZrSe_3$ is slightly lower and mostly isotropic, as shown in the inset in Fig. 7(a). For example, the $\kappa_L^{3ph}$ of $CaZrSe_3$ is 1.27, 1.16, and 1.08 $Wm^{-1}K^{-1}$ along *a*-, *b*-, and *c*-axis at 300 K, respectively. The anisotropy of $\kappa_L$ of orthorhombic $CaZrS_3$ mainly results from its anisotropic phonon group velocities. Specifically, its sound velocity along the *b*-axis is 4.6 km $s^{-1}$, which is ~1.5 times larger than that along the *a*-axis (3.3 km $s^{-1}$) and *c*-axis (3.2 km $s^{-1}$). In contrast, $CaZrSe_3$ exhibits mostly isotropic sound velocities, which are 3.6, 3.4, and 3.0 km $s^{-1}$ along *a*-, *b*-, and *c*-axis, respectively. All these values are the arithmetic averages of the group velocities of three acoustic phonon branches at Γ point. Figs. 7(b-d) further compares the $\kappa_L^{3ph}$ and $\kappa_L^{3ph+4ph}$ of orthorhombic $CaZrS_3$, as well as the $\kappa_L^{3ph}$ of $CaZrSe_3$, along the *a*-, *b*-, and *c*-axis, respectively. The reduction of $\kappa_L$ by four-phonon scattering is minor below 300 K, and increases substantially with temperature. For instance, the reduction of $\kappa_L$ along the *c*-axis by four-phonon scattering is only 7% at 200 K and increases to 23% at 900K. The four-phonon scattering becomes more important at higher temperatures because more phonons are excited at higher temperatures, allowing stronger four-phonon than three-phonon scattering because the former scales quadratically with phonon population while the latter is linear to the population.

We next look into the thermal conductivity contributed by acoustic and optical phonons in orthorhombic $CaZrS_3$, as shown in Fig. 8. Fig. 8(a) shows that four-phonon scattering results in similar suppression on the transport of acoustic and optical phonons, e.g., the average $\kappa_L$ contributed by acoustic (optical) phonons decreases by 11.6% (9.5%) at 300 K and 24.8% (21.8%) at 900 K due to the consideration of four-phonon process. The contribution of optical phonons to $\kappa_L$ is as high as nearly 50%, e.g., 48.2% at 300 K and 49.9% at 900 K, as shown in the inset of Fig. 8(a). This is because the phonon lifetime and group velocity of many optical phonons are comparable to those of acoustic phonons (Figs. S6 and S7). Specifically, the optical phonons within the frequency range 1.7-5.0 THz contribute to 40% of the total thermal conductivity at 300 K (see Fig. S8). This observation contradicts the general expectation that acoustic phonons

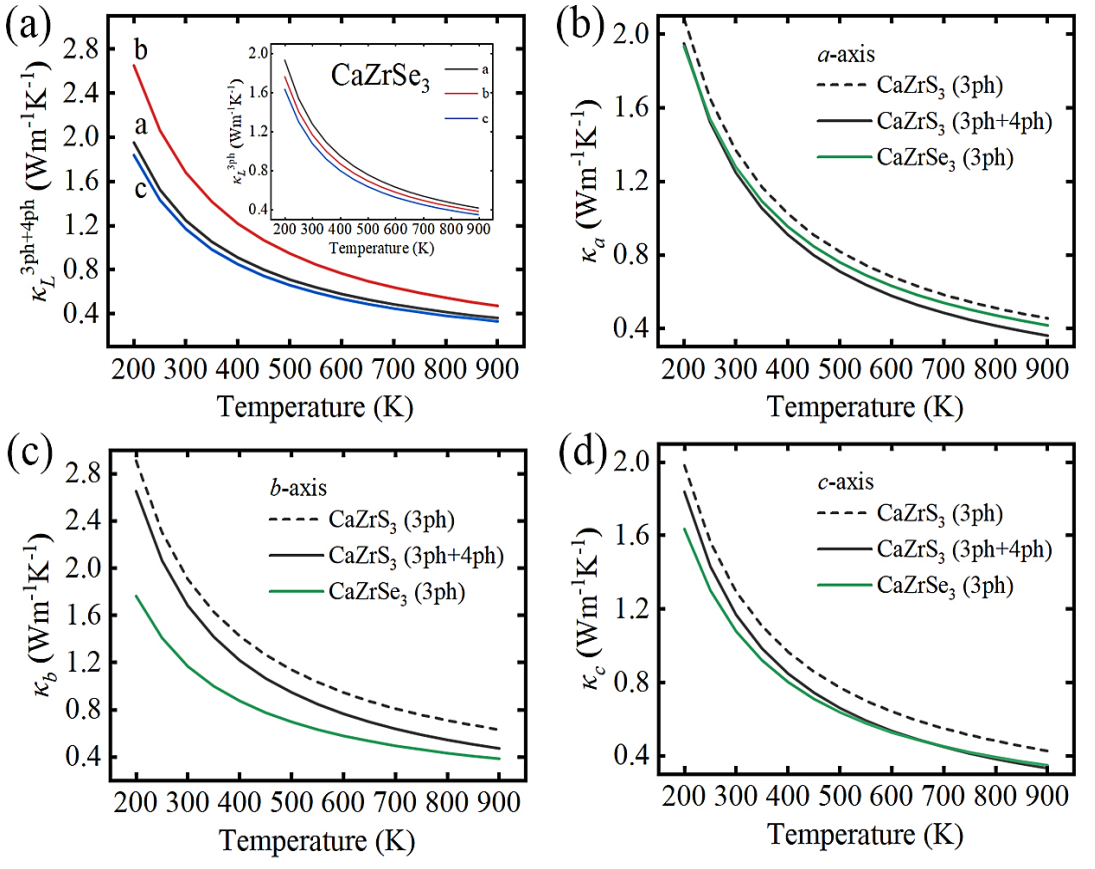


**Fig. 7** Thermal conductivity of orthorhombic $CaZrS_3$ calculated by GAP in comparison with $CaZrSe_3$. (a) Thermal conductivity as a function of temperature considering both three-phonon and four-phonon scattering along *a*-, *b*-, and *c*-axis for $CaZrS_3$. The inset shows the same results for $CaZrSe_3$. (b) Thermal conductivity considering only the three-phonon process for $CaZrS_3$ and $CaZrSe_3$, and that considering both three-phonon and four-phonon processes for $CaZrS_3$ along *a*-axis. (c) Same as (b) but along the *b*-axis, and (d) *c*-axis, respectively.

dominate thermal conduction in most bulk crystals. For instance, the acoustic phonons contribute ~95% to the $\kappa_L$ of bulk Si[76] and ~96.4% to the $\kappa_L$ of AlSb[77] at 300 K. Similarly high optical contribution to $\kappa_L$ has been observed in some other perovskite materials, e.g., the contribution of optical phonons to $\kappa_L$ is nearly 64% in $BaZrO_3$[74] and 71.5% in $SrTiO_3$.[78] It is also noticed that the relative $\kappa_L$ contribution of acoustic phonons decreases with temperature while that of optical phonons increases with temperature. This is expected because more excited optical phonons participate in thermal transport as temperature increases. A similar trend is observed for the relative contribution of acoustic and optical phonons to the $\kappa_L$ along each axis. For both $\kappa_b$ and $\kappa_c$, the optical phonons contribute relatively less to thermal conductivity than the acoustic phonons. In contrast, the contribution of optical phonons to $\kappa_a$ is relatively larger as compared to acoustic phonons, which can be ascribed to the larger group velocity of optical phonons along *a*-axis as shown in Fig. S4.

The low $\kappa_L$ of $CaZrS_3$ is featured by its short phonon MFP. In Fig. 9, we further plot the cumulative $\kappa_L$ of orthorhombic $CaZrS_3$ as a function of MFP at 300, 600, and 900 K. The MFP corresponding to 50% cumulative $\kappa_L$ along *b*-axis is almost twice as much as that along *a*-axis and *c*-axis. Also, the MFPs exhibit significant reduction as temperature increases. Specifically, the MFPs corresponding to 50% cumulative $\kappa_L$ along *a*-, *b*-, and *c*-axis decrease significantly as temperature increases from 300 K (4.6, 9.8, and 5.6 nm) to 600 K (1.8, 4.6, and 2.7 nm) and 900 K (1.1, 2.7, and 1.5 nm). The MFPs of orthorhombic $CaZrS_3$ at 300 K are close to those of other materials with similarly low $\kappa_L$, such as SnSe[79] and SnS[79] with an average $\kappa_L$ of 1.50 and 1.63 $Wm^{-1}K^{-1}$ at 300 K, respectively. The MFPs corresponding to 50% cumulative $\kappa_L$ are 5.6, 4.9, and 4.1 nm along the *a*-, *b*-, and *c*-axis for SnSe at 300 K, respectively, while those for SnS are 5.2, 4.3, and 4.0 nm. The short MFPs of orthorhombic $CaZrS_3$ suggest that nanostructuring would be difficult to further decrease its $\kappa_L$. We also notice the sharp increase of $\kappa_b$ around the MFP where the $\kappa_a$ and $\kappa_c$ saturate, which can be attributed to the contribution of the long-wavelength phonons resulting from the notably larger group velocities along the *c*-axis. The short MFPs in orthorhombic $CaZrS_3$ indicate its strong anharmonicity, which can be characterized by the Grüneisen parameters ($\gamma$). The calculated $\gamma$ of $CaZrS_3$ is 1.47 at 300 K, which is close to that of SnSe (2.12, 1.55, and 1.66 along *a*-, *b*-, and *c*-axis, respectively)[79] and SnS (2.17, 1.44, and 1.55 along *a*-, *b*-, and *c*-axis, respectively).[79] In comparison,

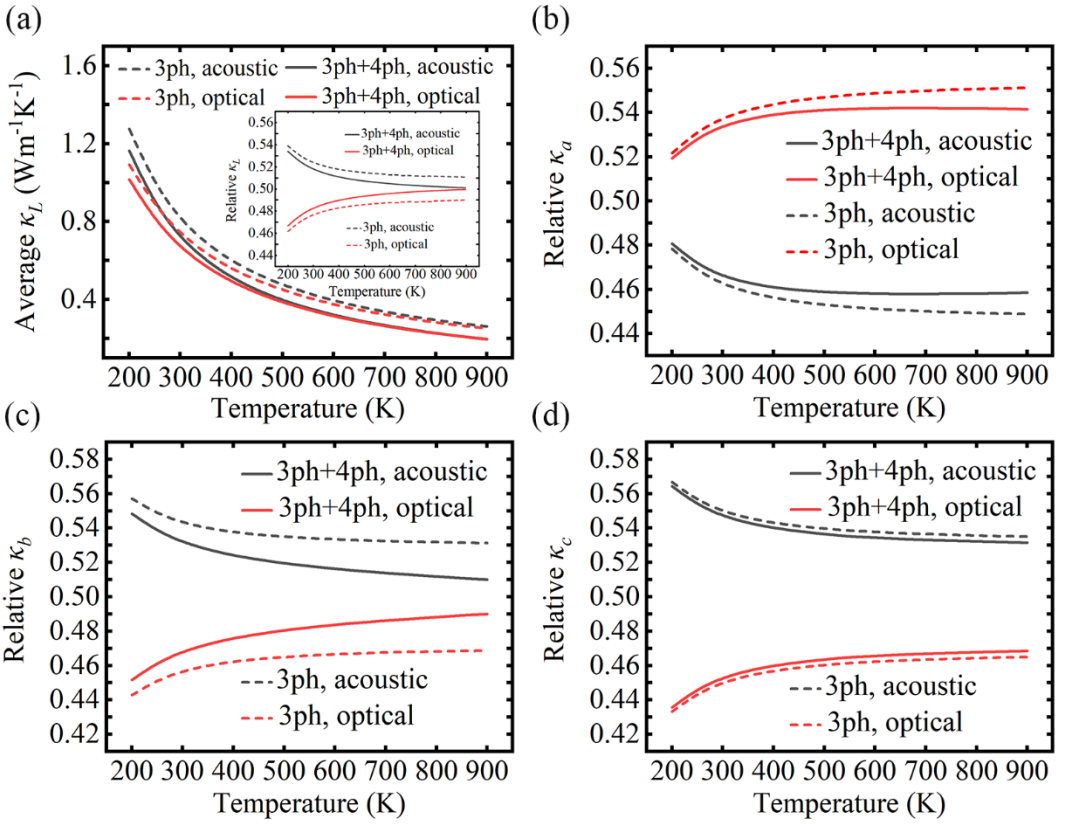


**Fig. 8** Comparison of thermal conductivity contributed by acoustic and optical phonons in orthorhombic $CaZrS_3$. (a) Average thermal conductivity considering only three-phonon process and both three-phonon and four-phonon processes as a function of temperature. The inset shows the relative contribution of acoustic and optical phonons to thermal conductivity. (b) The relative contribution of the thermal conductivity from acoustic and optical phonons along *a*-axis. (c) Same as (b) but along the *b*-axis and (d) *c*-axis, respectively.

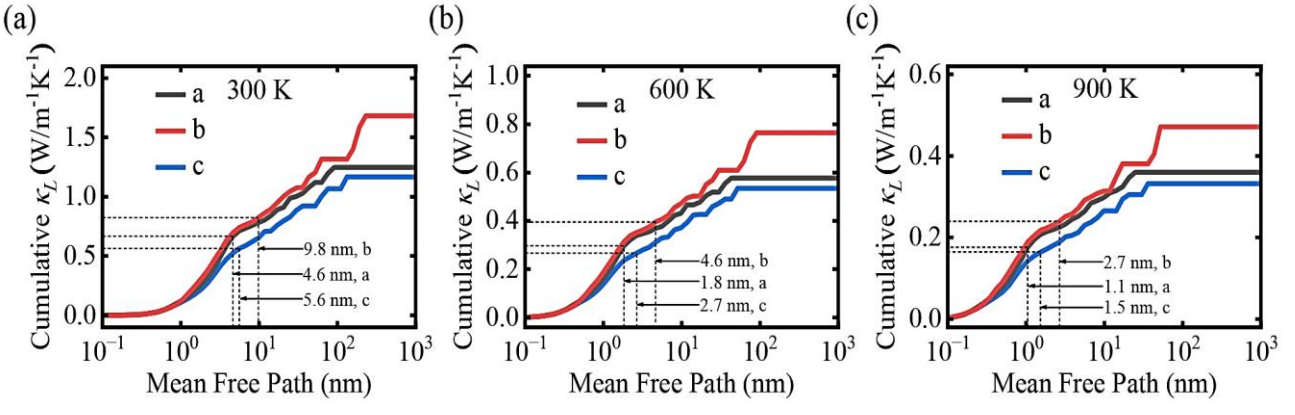


**Fig. 9** Cumulative thermal conductivity as a function of MFP in orthorhombic $CaZrS_3$. The calculated results along *a*-, *b*-, and *c*-axis at (a) 300, (b) 600, and (c) 900 K, respectively. The dashed lines denote the MFPs corresponding to 50% cumulative $\kappa_L$ along *a*-, *b*-, and *c*-axis, respectively.

$CaZrSe_3$ has relatively large γ (e.g., 3.75 at 300 K), which indicates stronger anharmonicity and rationalizes its relatively lower $\kappa_L$.

We now look into phonon transport details to understand the influence of four-phonon scattering on the $\kappa_L$ of orthorhombic $CaZrS_3$. Fig. 10 compares the three-phonon and four-phonon scattering rates at 300, 600, and 900 K, respectively. The four-phonon scattering rates are 1-2 orders of magnitude lower than three-phonon scattering rates at 300 K, which follows the general expectation of perturbation theory, i.e., higher-order terms of the Hamiltonian have smaller values and produce weaker phonon scattering. As temperature increases from 300 to 900 K, both the three- and four-phonon scattering processes become stronger while the latter one grows faster, explaining the stronger suppression of $\kappa_L$ by four-phonon scattering at high temperatures. This

 

observation obeys the scaling law derived for the four-phonon scattering ($\tau_4^{-1}\sim T^2\omega^4$), which is more strongly temperature dependent as compared to $\tau_3^{-1}\sim T\omega^2$ for the three-phonon scattering.

To gain a deeper understanding of phonon scattering, we further calculated the phase space of three-phonon and four-phonon scattering, as shown in Fig. 11. The three-phonon scattering channels can be decomposed into absorption process ($\lambda_1+\lambda_2\rightarrow\lambda_3$), and emission process ($\lambda_1\rightarrow\lambda_2+\lambda_3$) while the four-phonon scattering channels include recombination ($\lambda_1+\lambda_2+\lambda_3\rightarrow\lambda_4$), redistribution ($\lambda_1+\lambda_2\rightarrow\lambda_3+\lambda_4$) and splitting ($\lambda_1\rightarrow\lambda_2+\lambda_3+\lambda_4$) processes. In general, the phase space of the three-phonon absorption and emission processes decrease and increase with increasing phonon frequency, respectively, which can be mainly attributed to the constraint of energy conservation. We notice that the scattering rates resulting from the absorption and emission processes exhibit frequency dependence similar to the corresponding phase space, indicating the dominant role of phase space in determining the phonon scattering. As a result, the absorption and emission processes dominate the scattering below ~2.9 THz and above ~7.2 THz, respectively, while in between, the scattering rates from both processes are comparable. Similarly, for the four-phonon processes, the phase space and scattering rates of the recombination and splitting processes decrease and increase with increasing phonon frequency mainly due to the restriction of energy conservation. Compared with the three-phonon absorption (emission) process, the phase space of the four-phonon recombination (splitting) process is orders of magnitude lower throughout the entire frequency range, resulting in the correspondingly lower four-phonon scattering rates. In contrast, the phase space of the four-phonon redistribution process is much larger and comparable to that of the three-phonon processes for most frequencies. Therefore, the redistribution process dominates the four-phonon scattering rates within most frequency range. Although the phase space of the redistribution process is as large as that of the three-phonon processes, the scattering rates resulting from the redistribution process are substantially smaller than the corresponding three-phonon scattering rates, implying the contribution of the smaller fourth-order Hamiltonian.

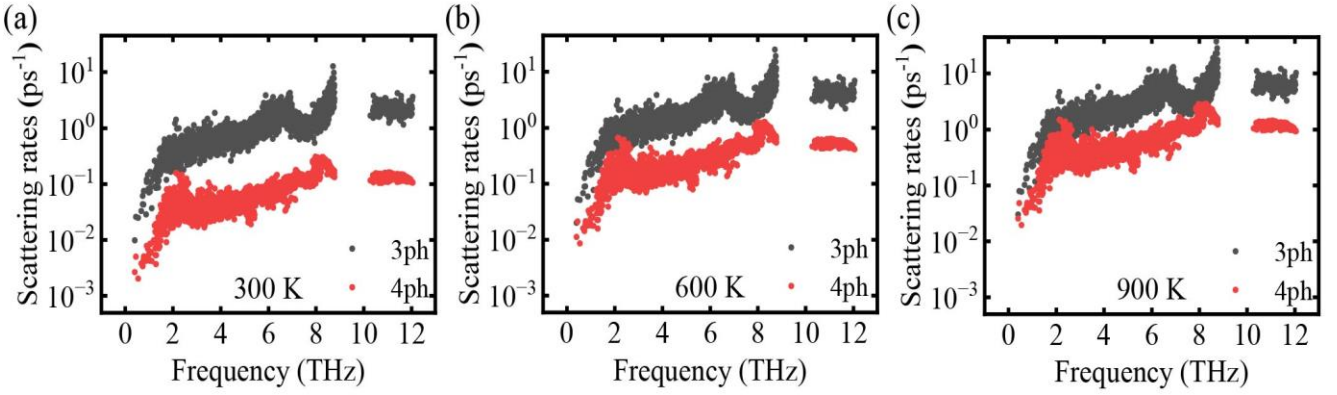


**Fig. 10** Phonon scattering rates of orthorhombic $CaZrS_3$. Three-phonon and four-phonon scattering rates as a function of phonon frequency at (a) 300 K, (b) 600 K, and (c) 900 K, respectively.

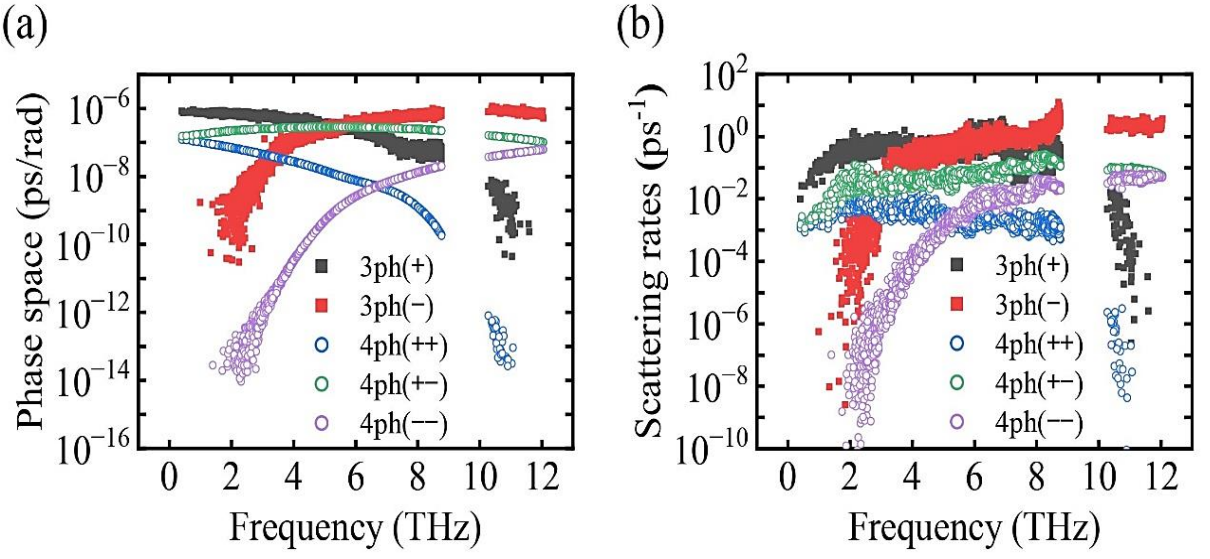


**Fig. 11** Phonon scattering channels of three-phonon and four-phonon processes in orthorhombic $CaZrS_3$. (a) Phase space as a function of phonon frequency. (b) The phonon scattering rates of different scattering channels as a function of phonon frequency at 300 K.

The relative magnitudes of the three-phonon and four-phonon phase space are essentially determined by phonon dispersion. According to previous studies, some unique features in phonon dispersion, such as the large a-o gap (the frequency gap between acoustic and optical phonons), acoustic bunching, and flat optical bands, can more strongly restrict the three-phonon as compared to the four-phonon processes and result in relatively stronger four-phonon scattering rates.[77,80,81] A typical example is BAs, for which the large a-o gap (~10 THz) and acoustic bunching largely weaken the three-phonon scattering.[80] As a result, four-phonon scattering results in ~36.8% reduction in the $\kappa_L$ of BAs at room temperature.[81] In contrast, the orthorhombic $CaZrS_3$ has a small frequency gap of ~1.5 THz in phonon dispersion, which has little restriction on the three-phonon and four-phonon processes. Another feature in its phonon dispersion is the bunching of optical branches, which makes the satisfaction of the energy and momentum conservation easier. This may explain the much larger phase space of the redistribution process as compared to the recombination and splitting processes. Similar observations have been reported for BAs,[77] AlSb,[77] and SnSe.[82]

## 4. Conclusion

In this work, we developed a high-quality GAP for describing both orthorhombic and cubic $CaZrS_3$, which achieves a DFT-level accuracy in predicting their structural and lattice vibrational properties. Specifically, we used the GAP to study the phonon transport properties in orthorhombic $CaZrS_3$ by considering both three-phonon and four-phonon scattering processes from 200 to 900 K. The $\kappa_L$ of orthorhombic $CaZrS_3$ (1.25, 1.68, and 1.17 $Wm^{-1}K^{-1}$ along *a*-, *b*-, and *c*-axis at 300 K) is similarly low but more anisotropic compared to its counterpart $CaZrSe_3$ (1.27, 1.16, and 1.08 $Wm^{-1}K^{-1}$ along *a*-, *b*-, and *c*-axis at 300 K). The low $\kappa_L$ of orthorhombic $CaZrS_3$ can be attributed to its strong anharmonicity. The relatively larger anisotropy of $\kappa_L$ in $CaZrS_3$ mainly results from its anisotropic group velocities, for example, the sound velocity along *b*-axis is 1.5 times as large as that along *a*- and *c*-axis. The low $\kappa_L$ of $CaZrS_3$ is featured by its short MFPs, with a value of 4.6, 9.8, and 5.6 nm corresponding to 50% cumulative $\kappa_L$ at 300 K along the *a*-, *b*-, and *c*-axis, respectively. Also, we find nearly half of the $\kappa_L$ is contributed by optical phonons throughout the entire temperature range. Particularly, the four-phonon scattering plays an important role in governing its thermal transport, especially at high temperatures. Specifically, the four-phonon scattering decreases its $\kappa_L$ by 10% at 300 K, while the reduction increases to 23% at 900 K. The four-phonon scattering is dominated by the redistribution process with a large phase space, which is comparable to that of three-phonon processes throughout most frequency range.

Our work demonstrates that GAP can be an accurate and efficient tool to study the thermal properties of ternary compounds. The insights gained into phonon transport of orthorhombic $CaZrS_3$ will be helpful for tailoring the thermal properties and thus the performance of perovskites for photovoltaics, optoelectronics, thermoelectrics, etc.

## Acknowledgments

We would like to thank the Shandong Institute of Advanced Technology for providing computational resources. This work is supported by the Excellent Young Scientists Fund (Overseas) of Shandong Province (2022HWYQ-091), the Taishan Scholars Program of Shandong Province, the Natural Science Foundation of Shandong Province (ZR2022MA011), and the Initiative Research Fund of Shandong Institute of Advanced Technology.

## Conflict of Interest

There is no conflict of interest.

## Supporting Information

Applicable

## References

[1] K. V. Sopiha, C. Comparotto, J. A. Márquez, J. J. S. Scragg, Chalcogenide perovskites: tantalizing prospects, challenging materials, *Advanced Optical Materials*, 2022, **10**, 2101704, doi: 10.1002/adom.202101704.

[2] A. Swarnkar, W. J. Mir, R. Chakraborty, M. Jagadeeswararao, T. Sheikh, A. Nag, Are chalcogenide perovskites an emerging class of semiconductors for optoelectronic properties and solar cell? *Chemistry of Materials*, 2019, **31**, 565-575, doi: 10.1021/acs.chemmater.8b04178.

[3] S. Perera, H. Hui, C. Zhao, H. Xue, F. Sun, C. Deng, N. Gross, C. Milleville, X. Xu, D. F. Watson, B. Weinstein, Y.-Y. Sun, S. Zhang, H. Zeng, Chalcogenide perovskites - an emerging class of ionic semiconductors, *Nano Energy*, 2016, **22**, 129-135, doi: 10.1016/j.nanoen.2016.02.020.

[4] W. Meng, B. Saparov, F. Hong, J. Wang, D. B. Mitzi, Y. Yan, Alloying and defect control within chalcogenide perovskites for optimized photovoltaic application, *Chemistry of Materials*, 2016, **28**, 821-829, doi: 10.1021/acs.chemmater.5b04213.

[5] P. Basera, S. Bhattacharya, Chalcogenide perovskites ($ABS_3$; A = Ba, Ca, Sr; B = Hf, Sn): an emerging class of semiconductors for optoelectronics, *The Journal of Physical Chemistry Letters*, 2022, **13**, 6439-6446, doi: 10.1021/acs.jpclett.2c01337.

[6] E. Osei-Agyemang, C. E. Adu, G. Balasubramanian, Ultralow lattice thermal conductivity of chalcogenide perovskite $CaZrSe_3$ contributes to high thermoelectric figure of merit, *Npj Computational Materials*, 2019, **5**, 116, doi: 10.1038/s41524-019-0253-5.

[7] Y.-Y. Sun, M. L. Agiorgousis, P. Zhang, S. Zhang, Chalcogenide perovskites for photovoltaics, *Nano Letters*, 2015, **15**, 581-585, doi: 10.1021/nl504046x.

[8] R. Yang, A. D. Jess, C. Fai, C. J. Hages, Low-temperature, solution-based synthesis of luminescent chalcogenide perovskite $BaZrS_3$ nanoparticles, *Journal of the American Chemical Society*, 2022, **144**, 15928-15931, doi: 10.1021/jacs.2c06168.

[9] E. Osei-Agyemang, C. Enninful Adu, G. Balasubramanian,

 

Doping and anisotropy-dependent electronic transport in chalcogenide perovskite $CaZrSe_3$ for high thermoelectric efficiency, *Advanced Theory and Simulations*, 2019, **2**, 1900060, doi: 10.1002/adts.201900060.
[10] Hua, Zhang, Effect of temperature on the efficiency of organometallic perovskite solar cells, *Journal of Energy Chemistry*, 2015, **24**, 729-735, doi: 10.1016/j.jechem.2015.10.007.
[11] K. Choi, J. Lee, H. Choi, G.-W. Kim, H. I. Kim, T. Park, Heat dissipation effects on the stability of planar perovskite solar cells, *Energy & Environmental Science*, 2020, **13**, 5059-5067, doi: 10.1039/d0ee02859b.
[12] E. Radziemska, The effect of temperature on the power drop in crystalline silicon solar cells, *Renewable Energy*, 2003, **28**, 1-12, doi: 10.1016/S0960-1481(02)00015-0.
[13] M. A. Haque, S. Kee, D. R. Villalva, W.-L. Ong, D. Baran, Halide perovskites: halide perovskites: thermal transport and prospects for thermoelectricity (adv. sci. 10/2020), *Advanced Science*, 2020, **7**, 2070056, doi: 10.1002/advs.202070056.
[14] H. Xie, S. Hao, J. Bao, T. J. Slade, G. J. Snyder, C. Wolverton, M. G. Kanatzidis, All-inorganic halide perovskites as potential thermoelectric materials: dynamic cation off-centering induces ultralow thermal conductivity, *Journal of the American Chemical Society*, 2020, **142**, 9553-9563, doi: 10.1021/jacs.0c03427.
[15] Y. Zhao, S. Zeng, G. Li, C. Lian, Z. Dai, S. Meng, J. Ni, Lattice thermal conductivity including phonon frequency shifts and scattering rates induced by quartic anharmonicity in cubic oxide and fluoride perovskites, *Physical Review B*, 2021, **104**, 224304, doi: 10.1103/physrevb.104.224304.
[16] C. Huh, W. J. Schaff, L. F. Eastman, S.-J. Park, Temperature dependence of performance of InGaN/GaN MQW LEDs with different indium compositions, *IEEE Electron Device Letters*, 2004, **25**, 61-63, doi: 10.1109/LED.2003.822659.
[17] A. Rashidi, M. Monavarian, A. Aragon, D. Feezell, Thermal and efficiency droop in InGaN/GaN light-emitting diodes: decoupling multiphysics effects using temperature-dependent RF measurements, *Scientific Reports*, 2019, **9**, 19921, doi: 10.1038/s41598-019-56390-2.
[18] G. J. Snyder, E. S. Toberer, Complex thermoelectric materials, *Nature Materials*, 2008, **7**, 105-114, doi: 10.1038/nmat2090.
[19] K. Biswas, J. He, I. D. Blum, C.-I. Wu, T. P. Hogan, D. N. Seidman, V. P. Dravid, M. G. Kanatzidis, High-performance bulk thermoelectrics with all-scale hierarchical architectures, *Nature*, 2012, **489**, 414-418, doi: 10.1038/nature11439.
[20] L.-D. Zhao, S.-H. Lo, Y. Zhang, H. Sun, G. Tan, C. Uher, C. Wolverton, V. P. Dravid, M. G. Kanatzidis, Ultralow thermal conductivity and high thermoelectric figure of merit in SnSe crystals, *Nature*, 2014, **508**, 373-377, doi: 10.1038/nature13184.
[21] B. Jiang, W. Wang, S. Liu, Y. Wang, C. Wang, Y. Chen, L. Xie, M. Huang, J. He, High figure-of-merit and power generation in high-entropy GeTe-based thermoelectrics, *Science*, 2022, **377**, 208-213, doi: 10.1126/science.abq5815.
[22] S. I. Kim, K. H. Lee, H. A. Mun, H. S. Kim, S. W. Hwang, J. W. Roh, D. J. Yang, W. H. Shin, X. S. Li, Y. H. Lee, G. J. Snyder, S. W. Kim, Dense dislocation arrays embedded in grain boundaries for high-performance bulk thermoelectrics, *Science*, 2015, **348**, 109-114, doi: 10.1126/science.aaa4166.
[23] E. Osei-Agyemang, G. Balasubramanian, Understanding the extremely poor lattice thermal transport in chalcogenide perovskite $BaZrS_3$, *ACS Applied Energy Materials*, 2020, **3**, 1139-1144, doi: 10.1021/acsaem.9b02185.
[24] H. Shahmohamadi, S. S. Naghavi, Sulfide perovskites for thermoelectricity, *ACS Applied Materials & Interfaces*, 2021, **13**, 14189-14197, doi: 10.1021/acsami.0c22842.
[25] N. A. Moroz, C. Bauer, L. Williams, A. Olvera, J. Casamento, A. A. Page, T. P. Bailey, A. Weiland, S. S. Stoyko, E. Kioupakis, C. Uher, J. A. Aitken, P. F. P. Poudeu, Insights on the synthesis, crystal and electronic structures, and optical and thermoelectric properties of $Sr_{1-x}Sb_xHfSe_3$ orthorhombic perovskite, *Inorganic Chemistry*, 2018, **57**, 7402-7411, doi: 10.1021/acs.inorgchem.8b01038.
[26] P. K. Schelling, S. R. Phillpot, P. Keblinski, Comparison of atomic-level simulation methods for computing thermal conductivity, *Physical Review B*, 2002, **65**, 144306, doi: 10.1103/physrevb.65.144306.
[27] J. E. Turney, E. S. Landry, A. J. H. McGaughey, C. H. Amon, Predicting phonon properties and thermal conductivity from anharmonic lattice dynamics calculations and molecular dynamics simulations, *Physical Review B*, 2009, **79**, 064301, doi: 10.1103/physrevb.79.064301.
[28] H. Bao, J. Chen, X. Gu, B. Cao, A review of simulation methods in micro/nanoscale heat conduction, *ES Energy & Environment*, 2018, **1**, 16-55, doi: 10.30919/esee8c149.
[29] B. Mortazavi, I. S. Novikov, E. V. Podryabinkin, S. Roche, T. Rabczuk, A. V. Shapeev, X. Zhuang, Exploring phononic properties of two-dimensional materials using machine learning interatomic potentials, *Applied Materials Today*, 2020, **20**, 100685, doi: 10.1016/j.apmt.2020.100685.
[30] A. Hashemi, R. Guo, K. Esfarjani, S. Lee, *Ab initio* phonon transport across grain boundaries in graphene using machine learning based on small dataset, *Physical Review Materials*, 2022, **6**, 044004, doi: 10.1103/physrevmaterials.6.044004.
[31] S. Arabha, A. Rajabpour, Thermo-mechanical properties of nitrogenated holey graphene ($C_2N$): a comparison of machine-learning-based and classical interatomic potentials, *International Journal of Heat and Mass Transfer*, 2021, **178**, 121589, doi: 10.1016/j.ijheatmasstransfer.2021.121589.
[32] F. Wang, H.-H. Wu, L. Dong, G. Pan, X. Zhou, S. Wang, R. Guo, G. Wu, J. Gao, F.-Z. Dai, X. Mao, Atomic-scale simulations in multi-component alloys and compounds: a review on advances in interatomic potential, *Journal of Materials Science & Technology*, 2023, **165**, 49-65, doi: 10.1016/j.jmst.2023.05.010.
[33] V. L. Deringer, M. A. Caro, G. Csányi, Machine learning interatomic potentials as emerging tools for materials science, *Advanced Materials*, 2019, **31**, 1902765, doi: 10.1002/adma.201902765.
[34] Y. Zuo, C. Chen, X. Li, Z. Deng, Y. Chen, J. Behler, G. Csányi, A. V. Shapeev, A. P. Thompson, M. A. Wood, S. P. Ong, Performance and cost assessment of machine learning

interatomic potentials, *The Journal of Physical Chemistry A*, 2020, **124**, 731-745, doi: 10.1021/acs.jpca.9b08723.
[35] A. P. Bartók, M. C. Payne, R. Kondor, G. Csányi, Gaussian approximation potentials: the accuracy of quantum mechanics, without the electrons, *Physical Review Letters*, 2010, **104**, 136403, doi: 10.1103/physrevlett.104.136403.
[36] G. Sivaraman, A. N. Krishnamoorthy, M. Baur, C. Holm, M. Stan, G. Csányi, C. Benmore, Á. Vázquez-Mayagoitia, Machine-learned interatomic potentials by active learning: amorphous and liquid hafnium dioxide, *Npj Computational Materials*, 2020, **6**, 104, doi: 10.1038/s41524-020-00367-7.
[37] J. Byggmästar, A. Hamedani, K. Nordlund, F. Djurabekova, Machine-learning interatomic potential for radiation damage and defects in tungsten, *Physical Review B*, 2019, **100**, 144105, doi: 10.1103/physrevb.100.144105.
[38] Ruiqiang, Guo, Small-data-based machine learning interatomic potentials for graphene grain boundaries enabled by structural unit model, *Carbon Trends*, 2023, **11**, 100260, doi: 10.1016/j.cartre.2023.100260.
[39] J. Tang, G. Li, Q. Wang, J. Zheng, L. Cheng, R. Guo, Competition between phonon-vacancy and four-phonon scattering in cubic boron arsenide by machine learning interatomic potential, *Physical Review Materials*, 2023, **7**, 044601, doi: 10.1103/physrevmaterials.7.044601.
[40] Jialin, Tang, Effect of four-phonon scattering on anisotropic thermal transport in bulk hexagonal boron nitride by machine learning interatomic potential, *International Journal of Heat and Mass Transfer*, 2023, **207**, 124011, doi: 10.1016/j.ijheatmasstransfer.2023.124011.
[41] A. P. Thompson, L. P. Swiler, C. R. Trott, S. M. Foiles, G. J. Tucker, Spectral neighbor analysis method for automated generation of quantum-accurate interatomic potentials, *Journal of Computational Physics*, 2015, **285**, 316-330, doi: 10.1016/j.jcp.2014.12.018.
[42] Z. Deng, C. Chen, X.-G. Li, S. P. Ong, An electrostatic spectral neighbor analysis potential for lithium nitride, *Npj Computational Materials*, 2019, **5**, 75, doi: 10.1038/s41524-019-0212-1.
[43] A. Rodriguez, Y. Liu, M. Hu, Spatial density neural network force fields with first-principles level accuracy and application to thermal transport, *Physical Review B*, 2020, **102**, 035203, doi: 10.1103/physrevb.102.035203.
[44] K. Lee, D. Yoo, W. Jeong, S. Han, SIMPLE-NN: an efficient package for training and executing neural-network interatomic potentials, *Computer Physics Communications*, 2019, **242**, 95-103, doi: 10.1016/j.cpc.2019.04.014.
[45] S. Alireza Ghasemi, A. Hofstetter, S. Saha, S. Goedecker, Interatomic potentials for ionic systems with density functional accuracy based on charge densities obtained by a neural network, *Physical Review B*, 2015, **92**, 045131, doi: 10.1103/physrevb.92.045131.
[46] G. C. Sosso, G. Miceli, S. Caravati, J. Behler, M. Bernasconi, Neural network interatomic potential for the phase change material GeTe, *Physical Review B*, 2012, **85**, 174103, doi: 10.1103/physrevb.85.174103.
[47] I. S. Novikov, K. Gubaev, E. V. Podryabinkin, A. V. Shapeev, The MLIP package: moment tensor potentials with MPI and active learning, *Machine Learning: Science and Technology*, 2021, **2**, 025002, doi: 10.1088/2632-2153/abc9fe.
[48] A. V. Shapeev, Moment tensor potentials: a class of systematically improvable interatomic potentials, *Multiscale Modeling & Simulation*, 2016, **14**, 1153-1173, doi: 10.1137/15m1054183.
[49] F. Wu, F. Zheng, W. He, X. Cao, T.-Y. Lü, Z.-Z. Zhu, S. Wu, Deep learning interatomic potential for Ca-O system at high pressure, *Physical Review Materials*, 2022, **6**, 103802, doi: 10.1103/physrevmaterials.6.103802.
[50] Han, Wang, DeePMD-kit: a deep learning package for many-body potential energy representation and molecular dynamics, *Computer Physics Communications*, 2018, **228**, 178-184, doi: 10.1016/j.cpc.2018.03.016.
[51] Yuzhi, Zhang, DP-GEN: a concurrent learning platform for the generation of reliable deep learning based potential energy models, *Computer Physics Communications*, 2020, **253**, 107206, doi: 10.1016/j.cpc.2020.107206.
[52] W. J. Szlachta, A. P. Bartók, G. Csányi, Accuracy and transferability of Gaussian approximation potential models for tungsten, *Physical Review B*, 2014, **90**, 104108, doi: 10.1103/physrevb.90.104108.
[53] P. Rowe, G. Csányi, D. Alfè, A. Michaelides, Development of a machine learning potential for graphene, *Physical Review B*, 2018, **97**, 054303, doi: 10.1103/physrevb.97.054303.
[54] A. P. Bartók, J. Kermode, N. Bernstein, G. Csányi, Machine learning a general-purpose interatomic potential for silicon, *Physical Review X*, 2018, **8**, 041048, doi: 10.1103/physrevx.8.041048.
[55] A.P. Bartók, R. Kondor, G. Csányi, On representing chemical environments, *Physical Review B*, 2013, **87**, 184115, doi: 10.1103/PhysRevB.87.184115.
[56] S. De, A. P. Bartók, G. Csányi, M. Ceriotti, Comparing molecules and solids across structural and alchemical space, *Physical Chemistry Chemical Physics*, 2016, **18**, 13754-13769, doi: 10.1039/c6cp00415f.
[57] G. Kresse, J. Furthmüller, Efficient iterative schemes for*ab initio*total-energy calculations using a plane-wave basis set, *Physical Review B*, 1996, **54**, 11169-11186, doi: 10.1103/physrevb.54.11169.
[58] M. Ernzerhof, G. E. Scuseria, Assessment of the Perdew-Burke-Ernzerhof exchange-correlation functional, *The Journal of Chemical Physics*, 1999, **110**, 5029-5036, doi: 10.1063/1.478401.
[59] B. Hammer, L. B. Hansen, J. K. Nørskov, Improved adsorption energetics within density-functional theory using revised Perdew-Burke-Ernzerhof functionals, *Physical Review B*, 1999, **59**, 7413-7421, doi: 10.1103/physrevb.59.7413.
[60] J. P. Perdew, K. Burke, M. Ernzerhof, Generalized gradient approximation made simple, *Physical Review Letters*, 1996, **77**, 3865-3868, doi: 10.1103/physrevlett.77.3865.
[61] A. P. Thompson, H. M. Aktulga, R. Berger, D. S. Bolintineanu, W. M. Brown, P. S. Crozier, P. J. in 't Veld, A. Kohlmeyer, S. G. Moore, T. Dac Nguyen, R. Shan, M. J. Stevens,

 

J. Tranchida, C. Trott, S. J. Plimpton, LAMMPS - a flexible simulation tool for particle-based materials modeling at the atomic, meso, and continuum scales, *Computer Physics Communications*, 2022, **271**, 108171, doi: 10.1016/j.cpc.2021.108171.

[62] H.-H. Wu, L.-S. Dong, S.-Z. Wang, G.-L. Wu, J.-H. Gao, X.-S. Yang, X.-Y. Zhou, X.-P. Mao, Local chemical ordering coordinated thermal stability of nanograined high-entropy alloys, *Rare Metals*, 2023, **42**, 1645-1655, doi: 10.1007/s12598-022-02194-9.

[63] F. Wang, L. Dong, H.-H. Wu, P. Bai, S. Wang, G. Wu, J. Gao, J. Zhu, X. Zhou, X. Mao, Enhanced nanocrystalline stability of BCC iron via copper segregation, *Progress in Natural Science: Materials International*, 2023, **33**, 185-192, doi: 10.1016/j.pnsc.2023.05.001.

[64] R. Guo, B. Huang, Approaching the alloy limit of thermal conductivity in single-crystalline Si-based thermoelectric nanocomposites: a molecular dynamics investigation, *Scientific Reports*, 2015, **5**, 9579, doi: 10.1038/srep09579.

[65] R. Guo, B. Huang, Thermal transport in nanoporous Si: Anisotropy and junction effects, *International Journal of Heat and Mass Transfer*, 2014, **77**, 131-139, doi: 10.1016/j.ijheatmasstransfer.2014.05.002.

[66] W. Li, J. Carrete, N. A. Katcho, N. Mingo, ShengBTE: A solver of the Boltzmann transport equation for phonons, *Computer Physics Communications*, 2014, **185**, 1747-1758, doi: 10.1016/j.cpc.2014.02.015.

[67] Zherui, Han, FourPhonon: An extension module to ShengBTE for computing four-phonon scattering rates and thermal conductivity, *Computer Physics Communications*, 2022, **270**, 108179, doi: 10.1016/j.cpc.2021.108179.

[68] A. Togo, I. Tanaka, First principles phonon calculations in materials science, *Scripta Materialia*, 2015, **108**, 1-5, doi: 10.1016/j.scriptamat.2015.07.021.

[69] S. Baroni, S. de Gironcoli, A. Dal Corso, P. Giannozzi, Phonons and related crystal properties from density-functional perturbation theory, *Reviews of Modern Physics*, 2001, **73**, 515-562, doi: 10.1103/revmodphys.73.515.

[70] A. Bartók, Gaussian Approximation Potential: an interatomic potential derived from first principles Quantum Mechanics, 2010.

[71] H. Babaei, R. Guo, A. Hashemi, S. Lee, Machine-learning-based interatomic potential for phonon transport in perfect crystalline Si and crystalline Si with vacancies, *Physical Review Materials*, 2019, **3**, 074603, doi: 10.1103/physrevmaterials.3.074603.

[72] D. Yoo, K. Lee, W. Jeong, D. Lee, S. Watanabe, S. Han, Atomic energy mapping of neural network potential, *Physical Review Materials*, 2019, **3**, 093802, doi: 10.1103/physrevmaterials.3.093802.

[73] Y. Ouyang, C. Yu, J. He, P. Jiang, W. Ren, J. Chen, Accurate description of high-order phonon anharmonicity and lattice thermal conductivity from molecular dynamics simulations with machine learning potential, *Physical Review B*, 2022, **105**, 115202, doi: 10.1103/physrevb.105.115202.

[74] J. Zheng, D. Shi, Y. Yang, C. Lin, H. Huang, R. Guo, B. Huang, Anharmonicity-induced phonon hardening and phonon transport enhancement in crystalline perovskite $BaZrO_3$, *Physical Review B*, 2022, **105**, 224303, doi: 10.1103/physrevb.105.224303.

[75] J. Zheng, D. Shi, S. Liu, Y. Yang, C. Lin, Z. Chang, R. Guo, B. Huang, Effects of high-order anharmonicity on anomalous lattice dynamics and thermal transport in fully filled skutterudite $YbFe_4Sb_{12}$, *Physical Review Materials*, 2022, **6**, 093801, doi: 10.1103/physrevmaterials.6.093801.

[76] X. Wang, B. Huang, Computational study of In-plane phonon transport in Si thin films, *Scientific Reports*, 2014, **4**, 6399, doi: 10.1038/srep06399.

[77] X. Yang, T. Feng, J. Li, X. Ruan, Stronger role of four-phonon scattering than three-phonon scattering in thermal conductivity of III-V semiconductors at room temperature, *Physical Review B*, 2019, **100**, 245203, doi: 10.1103/physrevb.100.245203.

[78] Q. Wang, Z. Zeng, Y. Chen, Revisiting phonon transport in perovskite $SrTiO_3$: Anharmonic phonon renormalization and four-phonon scattering, *Physical Review B*, 2021, **104**, 235205, doi: 10.1103/physrevb.104.235205.

[79] R. Guo, X. Wang, Y. Kuang, B. Huang, First-principles study of anisotropic thermoelectric transport properties of IV-VI semiconductor compounds SnSe and SnS, *Physical Review B*, 2015, **92**, 115202, doi: 10.1103/physrevb.92.115202.

[80] L. Lindsay, D. A. Broido, T. L. Reinecke, First-principles determination of ultrahigh thermal conductivity of boron arsenide: a competitor for diamond?, *Physical Review Letters*, 2013, **111**, 025901, doi: 10.1103/physrevlett.111.025901.

[81] T. Feng, L. Lindsay, X. Ruan, Four-phonon scattering significantly reduces intrinsic thermal conductivity of solids, *Physical Review B*, 2017, **96**, 161201, doi: 10.1103/physrevb.96.161201.

[82] W. Zhou, Y. Dai, J. Zhang, B. Song, T.-H. Liu, R. Yang, Effect of four-phonon interaction on phonon thermal conductivity and mean-free-path spectrum of high-temperature phase SnSe, *Applied Physics Letters*, 2022, **121**, 112202, doi: 10.1063/5.0103919.

[83] M. Oumertem, D. Maouche, S. Berri, N. Bouarissa, D. P. Rai, R. Khenata, M. Ibrir, Theoretical investigation of the structural, electronic and thermodynamic properties of cubic and orthorhombic $XZrS_3$ (X = Ba, Sr, Ca) compounds, *Journal of Computational Electronics*, 2019, **18**, 415-427, doi: 10.1007/s10825-019-01317-3.

[84] R. Lelieveld, D. J. W. IJdo, Sulphides with the $GdFeO_3$ structure, *Acta Crystallographica Section B Structural Crystallography and Crystal Chemistry*, 1980, **36**, 2223-2226, doi: 10.1107/s056774088000845x.